Local impact of load cycling on degradation in polymer electrolyte fuel cells

D. Garcia-Sanchez[1*], T. Morawietz[1,2,3], Pedro Gama da Rocha[1], R. Hiesgen[2], Pawel Gazdzicki[1], K. A. Friedrich[1,3]

[1] *German Aerospace Center (DLR), Institute of Engineering Thermodynamics, Pfaffenwaldring 38-40, 70569 Stuttgart, Germany*

[2]*University of Applied Sciences Esslingen, Department of Basic Science, 73728 Esslingen, Germany*

[3] *University of Stuttgart, Institute of Building Energetics, Thermal Engineering and Energy Storage (IGTE), Pfaffenwaldring 31, 70569 Stuttgart, Germany*

*corresponding author: Daniel.GarciaSanchez@dlr.de

Keywords: *Polymer electrolyte membrane fuel cell, automotive, dynamic load cycling, local degradation, Pt band.*

Abstract

Degradation mechanisms occurring during proton exchange membrane fuel cells (PEMFC) operation critically depend on the applied electrical load profile. In this work, durability tests were performed using different load cycling ranges. The tests include refresh procedures in order to recover temporary performance losses. *Operando* current density distribution measurements as well as electrochemical characterization techniques were applied to obtain essential data for understanding degradation behavior of the components of the membrane electrode assembly (MEA). The analysis is supported by scanning electron microscopy (SEM) and energy dispersive x-ray diffraction (EDX) analysis of MEA components. Dynamic load cycling has proven to lead to lower performance losses as compared to constant load operation. Moreover, reversible performance losses were associated with an

increased heterogeneity of the current density distribution along the flow field. Thereby, areas with high local current density exhibit particularly strong Pt band formation in the membrane linked with a thinning of the cathode catalyst layer.

1. Introduction

Proton exchange membrane fuel cells (PEMFCs) are considered as key technology to reduce greenhouse gas emissions. In recent years, significant progress has been done towards meeting the challenging cost, durability, and performance targets required for the use of PEMFCs in automotive applications.[1,2] However, one of the remaining challenges of PEMFCs is the limited durability of membrane electrode assemblies (MEAs) caused by numerous chemical and physical degradation effects.[3]

Specifically, PEMFC durability is still below the 2020 target for automotive application especially at low Pt loadings [4, 5]. Hence, In order to reach the durability goals, degradation of cell components has to be understood and mitigated. [6-8]

Degradation effects in the case of perfluorosulfonic acid (PFSA) membranes and ionomers in the catalytic layers are [9-11]: (i) membrane thinning leading to performance reduction due to increased hydrogen cross-over [12-14]; (ii) pinhole or crack formation resulting in critical cell failure; (iii) reduction of ionic conductivity due to side chain cleavage [15] or blocking of SO_3 groups of the ionomer by non-protonic cations. Degradation of electrodes (cathode catalyst layers) is caused by loss of electrochemically active surface area (ECSA) due to catalyst particle growth or dissolution [16] and corrosion of the carbon support [17, 18]. The gas diffusion layer (GDL) degrades by carbon corrosion and loss of hydrophobic agents like

polytetrafluorethylene (PTFE) resulting in worsening of water management capabilities and gas transport properties [19].

Automotive PEMFC application demands dynamic load profiles which cover a broad range of current densities. Thereby 100% load is usually assigned to a current density which yields around 650 mV cell voltage; i.e. a typical current density range reaches from open current voltage (OCV= 0.0 A cm^{-2}) to around 1.0 - 1.5 A cm^{-2}. Hence, during dynamic durability tests numerous processes are involved that lead to performance losses making data interpretation difficult [7].

The nonlinear dynamics of the PEMFCs requires new approaches for simultaneous state estimation, parameter identification, and fault reconstruction [20-22] that will help in the data interpretation. Therefore, a clear discrimination of different phenomena requires studying certain current density ranges separately. As a first approach the studied operation ranges were defined as (i) the activation region ranging from 0.0 to 0.2 A cm^{-2} and (ii) the ohmic region ranging from 0.2 to 1.0 A cm^{-2}. The mass transport region was not studied since high current densities required to clearly observing mass transport limitations are usually not applied in automotive application. Additional tests at constant current have been carried out to allow comparison between dynamic and constant operation. The performed experiments include operando local current density distribution measurements using segmented cell [23-28]. These investigations are crucial to understand water management [29-37], local degradation [38-39], fuel starvation [40-43], and influence of MEA components on cell performance [44-48]. In the literature [49-53], load cycling was studied by using different load profiles, such as square wave or triangular wave potential perturbations. Since square wave is considered as most relevant for

an automotive dynamic load profile which required rapid load changes, in this work square wave profiles were used.

2. Experimental details

The effect of load cycling on degradation was studied in a single cell with 5x5 cm^2 active area and a gold coated single channel serpentine flow field arranged in co-flow configuration. The cell and the test bench were developed in-house at the German Aerospace Center (Deutsches Zentrum für Luft- und Raumfahrt e.V., DLR). It is equipped with programmable logic controllers (PLCs) and commercial electronic loads. The gas mass flow rates were regulated at the cell inlets whereas the pressure was controlled at the cell outlets. The absolute cell outlet pressure was fixed for the experiment at a constant value of 150 kPa (absolute pressure). The relative humidity of 50% of the feed gases was set by adjusting the dew point temperatures of the bubbler humidifiers at 64°C and keeping the cell temperature at 80°C. The tubings of the inlet gases were kept at temperatures 5°C higher than cell temperature in order to avoid water condensation.

Electrochemical impedance spectroscopy (EIS) and cyclic voltammetry (CV) was conducted using a PP241 potentiostat in a ZAHNER ZENNIUM electrochemical workstation with THALES software.

The current densities distributions where monitored using DLR's printed circuit board (PCB) [54] [55]. The segmentation of the PCB (segmented cell) with integrated flow field was installed at the anode side, see Figure 1(A). The board contains 6

integrated temperature sensors and is divided in 49 segments, each with an integrated current sensor (resistor).

The MEAs used in this study consisted of commercial MEA0476 catalyst coated membranes (CCMs) from Johnson Matthey Fuel Cells® and Sigracet 25 BC gas diffusion layers (GDL) from SGL Carbon GmbH. The cells were sealed with Ice Cube gaskets from Freudenberg®.

Testing protocols and electrochemical characterization

Once assembled, the cells were subject to the test protocol illustrated in Figure 1(B) consisting of:

(1) Start-up and breaking-in:

Cell operation was set to nominal conditions (80°C, 50%RH, 150 kPa_{abs}, 1.5 (H2)/2.0 (air) stoichiometry). Cell voltage and current density distribution were monitored at 1 A cm^{-2} for 1 hour for stabilization.

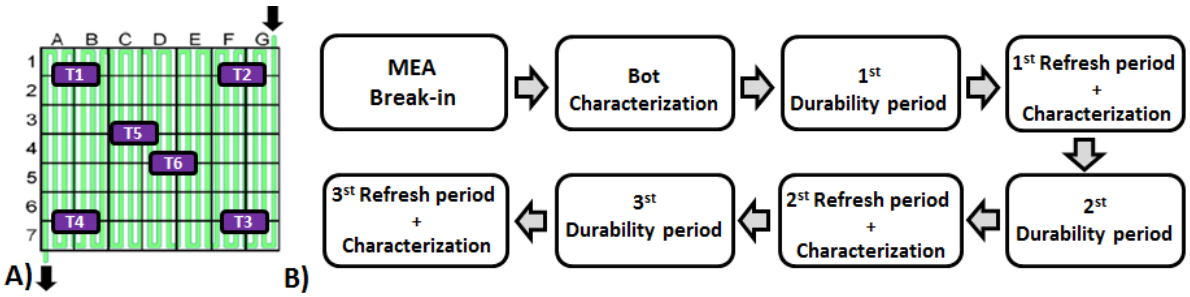

Figure 1 – (A) Segmentation of the anode flow field. As cathode the same single channel serpentine flow filed was used but without segmentation. The flow arrangement is co-flow. The labels of columns A-G and rows 1-7 are coordinates of the individual segments. Gas inlet is placed in the segment G1 and the gas outlet is located in A7 marked with arrows. (B) Schematized representation of the durability test.

(2) Characterization (BoT and EoT):

After break-in a set of electrochemical measurements defined as beginning of test (BoT) characterization was carried out. The same characterization techniques were applied at end of test (EoT). Specifically, a performance curve was measured starting from 0.0 Acm^{-2} up to 1.8 A cm^{-2}. To avoid dry out of the MEA in the current density range 0.0 – 0.2 A cm^{-2} the gas flows at anode and cathode were kept at a constant minimum flow rates of at 53 and 166 m min^{-1}, respectively. Above 0.2 A cm^{-2} the respective gas flows were set according to stoichiometry ratios of 1.5 and 2.0. The BoT cell performance of the tested MEA is provided in Figure 2.

Electrochemical impedance spectroscopy (EIS) measurements were performed at nominal operating conditions in galvanostatic mode at 0.1 and 0.6 A cm^{-2} in a frequency range from 100 mHz to 100 kHz.

Cyclic voltammetry (CV) measurements were conducted for both anode and cathode at ambient pressure and 80 °C using fully humidified gases (100% RH) at ambient temperature. The test electrode was fed by nitrogen at a flow rate of 100 ml min^{-1}, while the counter electrode was fed with hydrogen at 50 ml min^{-1}. Five subsequent cycles were performed in the potential range from 60 mV to 1 V at a sweep rate of 20 mV s^{-1}. The starting point of each cycle was at 400 mV. The ECSA was calculated using the equation ECSA = Q_{Pt} / (Γ x A) with the hydrogen adsorption charge on platinum Q_{Pt} corresponding to the area of the H_2 desorption peak, the charge required to reduce a monolayer of protons on platinum Γ = 210 µC cm^{-2} and the geometric active area A of the examined electrode.

(3) Operation period

After electrochemical characterization the MEA was subjected to durability testing, which consists of three periods of continuous PEMFC operation using the protocols provided in Figure 2 each lasting approximately 140 h. Between the operation periods a refresh procedure was applied in order to recover reversible voltage losses. The refresh procedure corresponds to shutting down the test cell, i.e. switching off electrical load, stopping gas supply, releasing pressure and letting the cell cooling down to room temperature for approximately 12 hours. After the third operation period a final refresh procedure was carried before performing the EoT characterization.

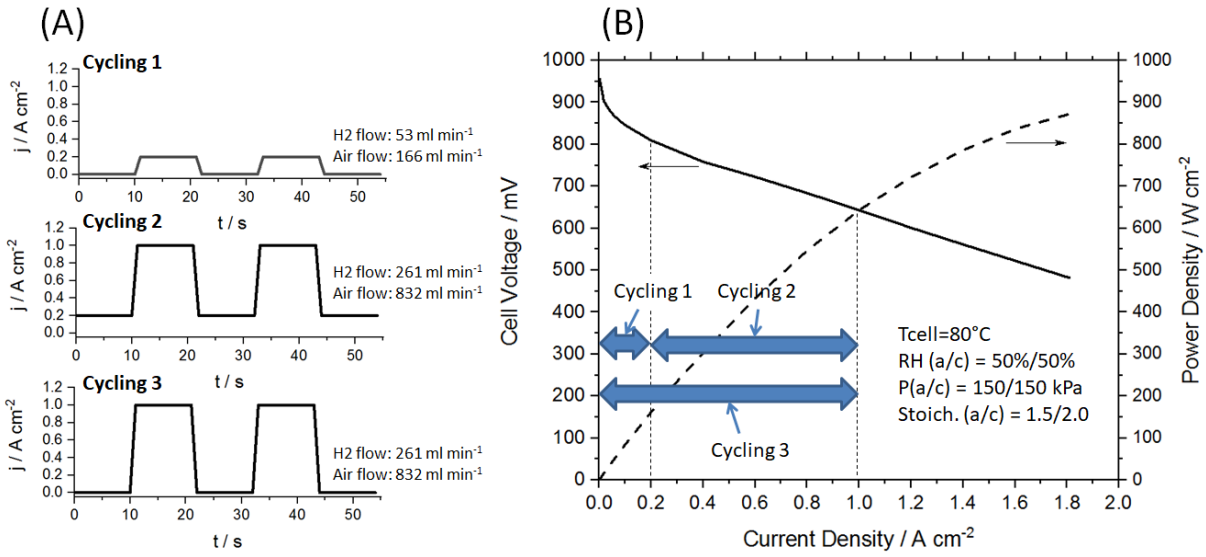

Figure 2: (A): Load cycling profiles applied in this study. (B): Ranges of load cycles related to the BoT performance curve of the tested MEA.

Ex-situ characterization

Analyses of the freeze fractured MEA samples were performed by scanning electron microscopy (SEM) and energy dispersive X-ray spectroscopy (EDX) using a JEOL JSM7200F device equipped with a Bruker Quantax energy dispersive X-ray analysis detector. On the SEM sample holder, the MEA samples were stabilized and electrically connected with double-sided conductive adhesive tape (Plano). The platinum content was analyzed as surface area fraction of the backscatter electron detector (BSE) images using the software ImageJ.

3. Results and Discussion

In order to study the impact of load cycling on degradation mechanisms, three different load cycles covering three different load ranges were tested to cover the nominal operation range of a PEMFC. It is noted that a fresh MEA was used for each cycling experiment. The applied cycles are:

- Cycling 1 (Cycling in the activation region of the performance curve): Load variation between 10 s at OCV and 10 s at 0.2 A cm^{-2} at constant gas flows of 53 ml min^{-1} (H_2) and 166 ml min^{-1} (air) at 50% RH, a cell temperature of 80°C and at 150 kPa absolute pressure.

- Cycling 2 (cycling in the ohmic region of the performance curve): Load variation between 10s at 0.2 A cm^{-2} and 1 A cm^{-2} at constant gas flows of 261 ml min^{-1} (H_2) and 832 ml min^{-1} (air) at 50% RH, a cell temperature of 80°C and at 150 kPa absolute pressure.

- Cycling 3 (cycling in the entire nominal operation range): Load variation between 10s at OCV and 1 A cm^{-2} at constant gas flows of 261 ml min^{-1} (H2) and 832 ml min^{-1} (air) at 50% RH, a cell temperature of 80°C and at 150 kPa absolute pressure.

Figure 3 (A) shows the voltage evolution measured for the three load cycles. In all cases the transition time between load levels was 1s.

Maximum applied current density in the cycling experiments is 1 A cm^{-2} which corresponds to 650 mV cell voltage which is a typical value for nominal automotive operation.

Additionally, Figure 3 (Right panels) depicts the mapping of the current density distributions recorded during the individual tests at BoT as well as before and after final refresh. A complete set of current density distribution images is provided in the Supporting Information Figure 1S.

The following parameters were evaluated from the test bench and electrochemical analysis:

- The irreversible/reversible degradation rates were calculated from the polarization curves at BoT and after each refresh.
- The Electrochemically Active Surface Area (ECSA) losses were calculated from the CV at BoT and after each refresh.
- The changes in impedances were evaluated from EIS and from the slope of the polarization curves at BoT and after each refresh.

The degradation tests performed using the three cycling protocols (Figure 3 (A)) show decreasing cell voltage as a function of operation time. The total number of

load cycles in the Cycling 1, Cycling 2, and Cycling 3 tests are 78,550 cycles, 62,200 cycles and 68,700 cycles, respectively.

Recoverable performance losses between the end of each period and the beginning of the next one are clearly observed. This fact suggests that the overall voltage degradation comprises two kinds of degradation process one being reversible and the other being irreversible.

The mappings of current density distributions, measured at the beginning and the end of each period show significant changes, i.e. the current density distributions become slightly heterogeneous during operation. During Cycling 1 and 2 and at low currents (0.2 A cm^{-2}), performance drops were measured in the areas close to the gas inlets corresponding to column G of the segmented cell (see Figure 1). Since the humidity of inlet gases was set to 50%, performance drop in gas inlet area can be explained due to drying caused by the high flows of the unsaturated gases. This effect does not occur in the cell center and outlet because drying is prevented by accumulation of product water along the low field. The condition change along the channel due to the change in the water uptake capacity is caused by water absorption [32,36]**.**

The inhomogeneities of the current density distributions observed after each period largely disappears after the refresh procedure. This recovery is not complete, and, especially in the last test period, irreversible mechanisms gain more importance and the inhomogeneities become only partly recovered. These irreversible losses are concurrent with the increase of the high and low frequencies resistances measured by EIS as will be shown in next section.

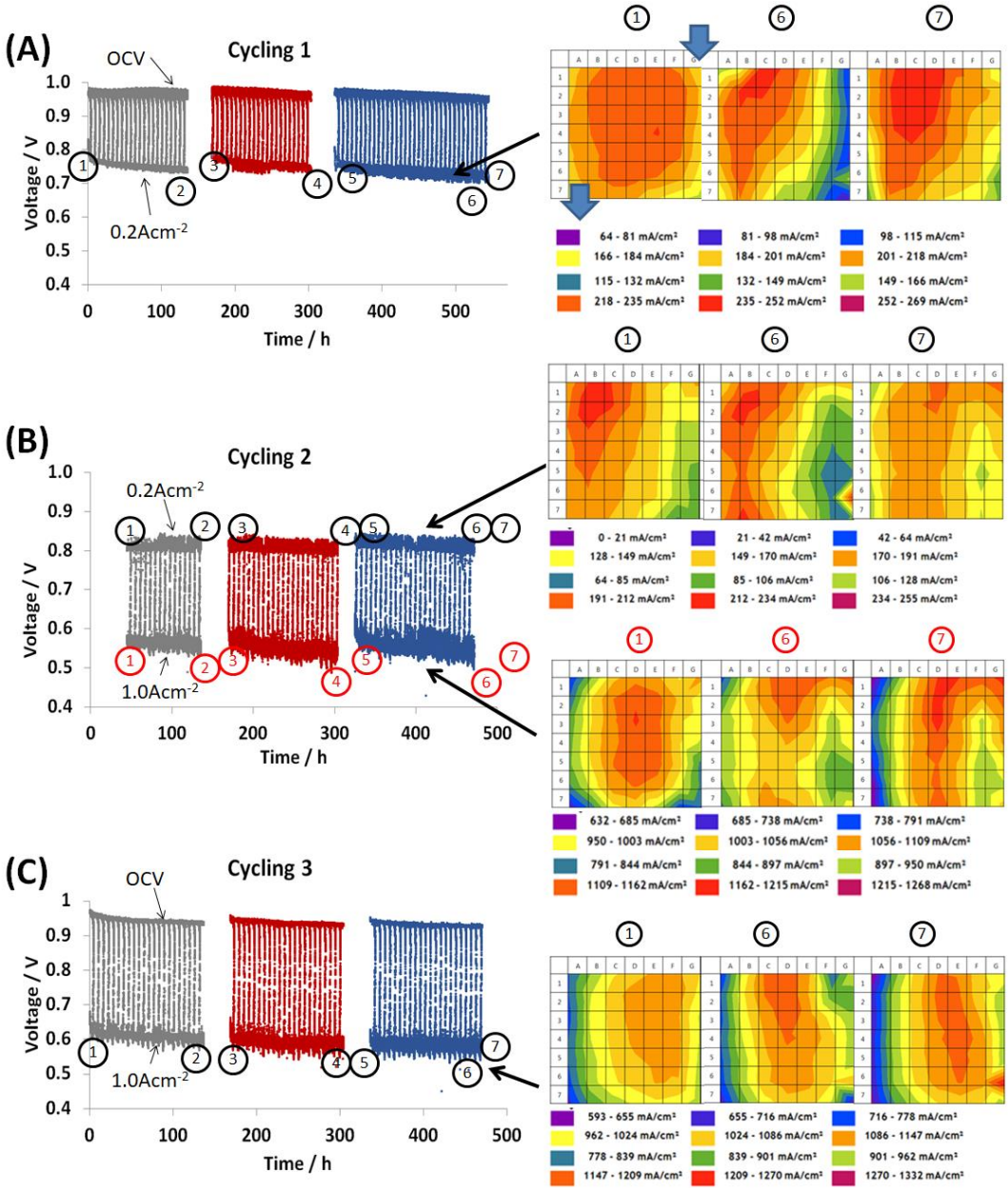

Figure 3: (Left:) Cell voltage versus test duration recorded using the load profiles Cycling 1 (A), Cycling 2 (B), and Cycling 3 (C). (Right:) Corresponding current density distributions recorded during the test at BoT (Nr. 1), before (Nr. 6) and after final refresh (Nr. 7, EoT). The assignment of the acquisition time of the current density image and the test is provided by the number labels. Gas inlet and outlet of the cell is located at segment G1 and A7, respectively.

In the first two test periods of Cycling 2 and 3 at high current density (1 Acm^{-2}) similar trends in the current inhomogeneities are observed. Thereby, the changes at the gas inlet (column G of the segmented cell) are less significant at high current than at 0.2 A cm^{-2}. In the last test period, however, outlet regions (column A of the segmented cell) exhibit performance losses most probably due to starvation processes at higher currents. It is noted that the gas flows were maintained constant at 261 $ml_{H2}min^{-1}$ and 832 $ml_{Air}min^{-1}$ during Cycling 2 and Cycling 3 corresponding to respective stoichiometries of 1.5 and 2 at a current density of 1 Acm^{-2}. Consequently, during periods of low load operation which corresponds to 50% of the operation time (see Figure 2) the stoichiometries were significantly higher; e.g. during operation at 0.2 A cm^{-2} the values equal to 7.5 and 10.0, respectively. During Cycling 3 in the flow field center areas (columns C, D and E) the currents are higher than 1 Acm^{-2} (Figure 3). Consequently, the local stoichiometry values were below 1.1 and 1.6 for H_2 and Air, respectively. The inhomogeneous in the current distribution produce local degradation effects that will be evaluated in the next sections.

Determination of Degradation Rates

The performance curves were measured for the three cycling tests at BoT, before and after each refresh as well as at EoT. The corresponding data is plotted in Figure 2S in the supporting information. The irreversible degradation rates (voltage loss per time) were calculated from the performance curves at BoT and after each refresh. This allows the determination of degradation rates as a function of current density as shown in Figure 4 (A). Additionally, corresponding irreversible degradation rates from

two tests conducted at a constant current density of 0.1 and 1.0 A cm^{-2} (data is not shown; the tests consist of three periods of operation interrupted by analogous recovery procedure as used with the cycling tests) are added. Apparently, the irreversible degradation rates of the cycling tests are significantly lower than those measured at constant load. In all cases the degradation rate increases with increasing current density. In particular, Cycling 1 which includes operation at high voltage only, exhibits significantly higher degradation than Cycling 2 and Cycling 3. This difference is due to specific degradation mechanisms promoted at these high voltage conditions (i.e. high cathode potential). At OCV the production rate of radicals is increased [58]. These radicals (·OH, HO_2) can attack the ionomer side chains or remaining carboxy groups at the PFSA backbone in the catalytic layers and/or the membrane. The proton transport properties of the ionomer become affected due to the loss of side-groups leading to an increase ohmic (HFR) resistance (compare Figure 5 (B)). The attack of the backbone would lead to reduction of mechanical stability of the membrane. A thinning of the membrane may be observed. However, SEM measurements (Figure 9S) indicate member thinning only for the Cycling 2 sample, which is the only cycle without OCV. Hence, this counter-intuitive observation must be due to another mechanism. A possible explanation could be the mitigation of membrane degradation by Pt precipitates in the membrane. Since the amount of Pt precipitates (Pt density [13] in the membrane is lowest for Cycling 2 (see Figure 7), it is more prone to degradation than Cycling 1 and 3. Also, carbon corrosion is accelerated at higher potentials. Furthermore, Pt advances the corrosion rate of carbon; when Pt is available, CO adsorbs on Pt and is oxidized between 0.6 and 0.8V to CO_2 [59]. Oxidized carbon is more hydrophilic and may decrease the mass transport [59]. As a second result of carbon corrosion Pt particles can detach

from the support and are not electronically connected to the electrical path. Correspondingly, Pt dissolution is potential dependent; higher dissolution rates are observed at higher potentials [60]. These factors may contribute to the high degradation of Cycling 1.

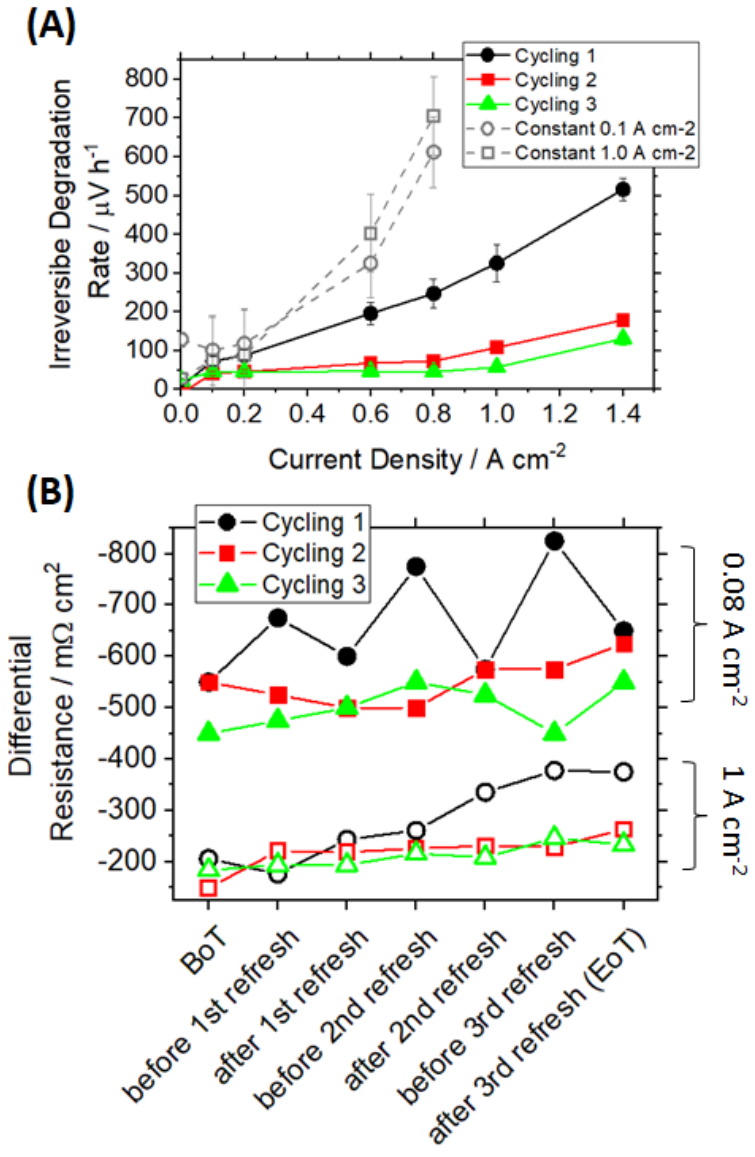

Figure 4: (A) Irreversible degradation rates calculated from the performance curves at BoT and after each refresh. Additionally, irreversible degradation rates from two tests conducted at a constant current density of 0.1 and 1.0 A cm^{-2} are added. (B) Differential resistance (slope of performance curve) calculated from the performance curves at 0.08 and 1.0 A cm^{-2}.

In order to visualize the reversibility of the degradation in the cycling tests, the differential resistances were calculated from the polarization curves at 1 A cm^{-2} and 0.08 A cm^{-2} representative for the ohmic and the activation region of the performance curves, respectively. Thereby, differential resistance $R_{diff}(j) = dU/dj$ is defined as the slope of the performance curve at a given current density j with U being the cell voltage. The differential resistances evaluated at BoT, before and after each refresh are depicted in Figure 4 (B). The differential resistance at 1 A cm^{-2} continuously increase with test duration; the strongest increase, which is consistent with the high degradation rate, is observed for Cycling 1. The increase of the differential resistance at 1 A cm^{-2} corresponds to an increase of ohmic losses of the MEA which are related to increasing membrane and interfacial resistances. More pronounced differences between Cycling 1 and Cycling 2 and 3 occur at 0.08 Acm^{-2}. For Cycling 1 a strong increase of differential resistance in the activation region develops during each operation period. This effect is partly reversible, i.e. the refresh procedures are clearly linked with a reduction of this resistance. Consequently, Cycling 1 leads to severe reversible degradation in the activation region of the polarization curve likely related to temporal catalyst passivation. It is noted that CV analysis was performed only at BoT and after each refresh, so there is no CV data to support the catalyst passivation hypothesis due to the recovery procedure.

Electrochemical characterization

CVs measurements of the anode and cathode electrodes of the samples have been recorded at BoT and after each refresh. The results in Figure 5 (A) show relative ECSA losses between BoT and EoT. Apparently, the relative ECSA losses are more pronounced on the cathodes than on the anodes which are expected due to the higher cathode potential. Interestingly, the ECSA losses at constant operation are lower than of the cycling tests even though the degradation rates of the MEAs operated at constant loads were much higher. Hence, ECSA loss cannot be considered as a main reason for the observed performance degradation. However, it could become an important issue for longer operation times when the ECSA decrease to critical levels. It is noted that the observed ECSA loss is not just an effect of the breaking-in of the MEAs that usually occurs during the first operation hours. Rather, the decrease of ECSA is a continuous process as evidenced by Figure S2 in the supporting information. One mechanism of the cathodic ECSA loss is platinum dissolution and migration from the cathode to the membrane that will be discussed later. Possibly the precipitation and growth of platinum in the anode side may be the reason for the minimal relative catalyst loss on this side[61].

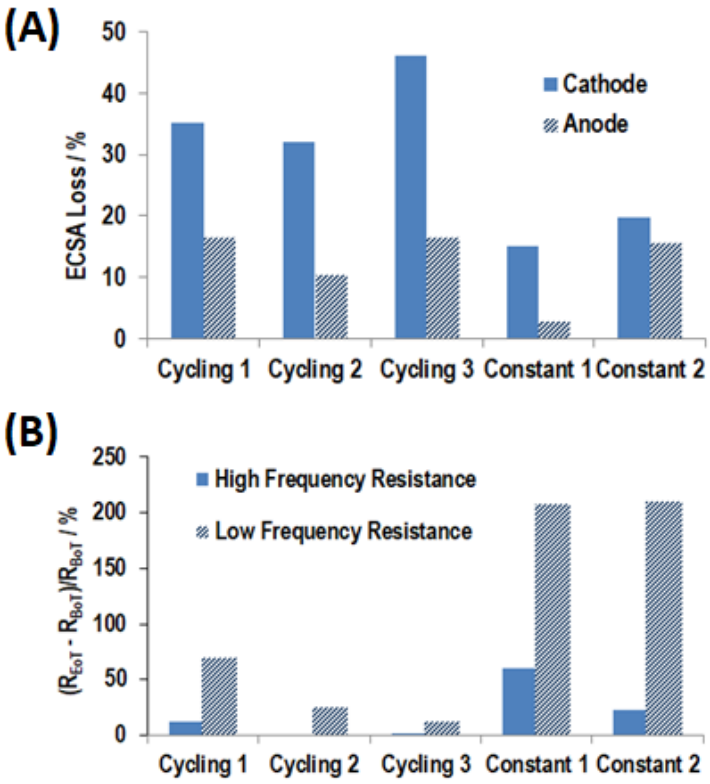

Figure 5: (A) Relative changes of anode and cathode ECSA between BoT and EoT. (B) Relative low frequency (LFR) and high frequency resistance (HFR) changes between the BoT and the EoT for the different samples. HFR and LFR are determined by the intersection with the real axis in the Nyquist diagrams at high and low frequencies. The corresponding EIS measurements were performed at 0.6 A cm^{-2}.

Changes of resistances R due to different degradation process of the tested cells were investigated using electrochemical impedance spectroscopy at 0.6 A cm^{-2} after each refresh period. Figure 5 (B) shows the relative increase of the high (HFR) and low frequency resistances (LFR) between BoT and EoT determined from the intercept of the Nyquist diagrams with the real impedance axis at low and high frequency (see in Figure 4S in the supporting information). While Cycling 1 shows a clear growth in HFR between BoT and EoT (approx. 12%), negligible differences

(<1%) were measured for Cycling 2 and 3. Since the EoT analysis is done after a refresh, this observation is linked with irreversible degradation which is particularly strong in case of constant operation test. A possible reason could be damage in the membrane side chain leading to reduced proton conductivity as discussed above. In case of LFR, significant differences were measured between BoT and EoT .Thereby, the effect is clearly larger in case of constant operation compared to load cycling. Among the load cycling tests, Cycling 1 shows the strongest increase in LFR. In this case, the high cell voltage maintained during operation likely induced carbon corrosion in the cathode catalyst layer as well in the porous media. The corrosion of the carbon media has particularly high impact when the cell is operated at high currents where proper gas supply and removal of product water play major roles regarding the cell performance. Once the carbon structure is degraded the cell suffers due to increased mass transport resistance. This finding agrees with the performance curves showing strong mass transport losses (see Figure 1S in the supporting information) and with results shown in Figure 4 (A); i.e. increase of HFR correlates well with the irreversible degradation rates observed at high current densities.

Local degradation analysis

To evaluate the structural degradation of the cycled cells, selected segments (A5, D5 and G5) have been cut out of the MEAs after EoT for SEM analysis. When using the backscattered electron detector (BSD) heavy elements appear brighter in the image compared to light elements. Therefore, Pt and carbon/polymer can be easily distinguished. The freeze-fractured MEAs of all analyzed samples from the cycling and constant load tests show Pt particles in the membrane. The Pt re-deposits were

detected close to the cathode side as shown in Figure 6 (B) as an example. The Pt content in front of the cathode was analyzed at areas of 15 x 15 µm² provided in Figure 6 (E) for different segments as binarized images after the different durability tests. It is known from literature [62,63] that in fuel cell operation due to numerous reasons (temperature, particle size, pH and potential), Pt dissolves even at lower potentials than expected from the stability limit given in the Pourbaix diagram of Pt. The dissolved platinum diffuses/migrates across the membrane and can be reduced to Pt by hydrogen that permeates through the membrane from the anode side. The position of the Pt inside the membrane is thus defined by the partial pressures of hydrogen and oxygen which determines the local potential inside the membrane [64]. To proof the particles visible in the images consist of Pt, EDX mapping (see Figure 6 (C)), EDX spectrum analysis (Figure 5S in the supporting information) and EDX Pt line-scans (Figure 4S in the supporting information) were recorded. A high magnification of the platinum particles is shown in Figure 6 (D). Differences in particle size were detected with the smallest particles occurring after Cycling 2. The particle size distributions can be found in Figure 10S in the Supporting Information. The redeposited particles formed spherical agglomerates or a crystal structure. Dendrite growth occurred in case of bigger particles as shown in Figure 6 (D) and Figure 7S in the supporting information. It should be noted that due to the limited resolution SEM very small particles are hardly detected but might be present. Interestingly, in segment A5 of Cycling 3 platinum particles are also detected in the membrane at the anode side (see Figure 8S in the Supporting Information).

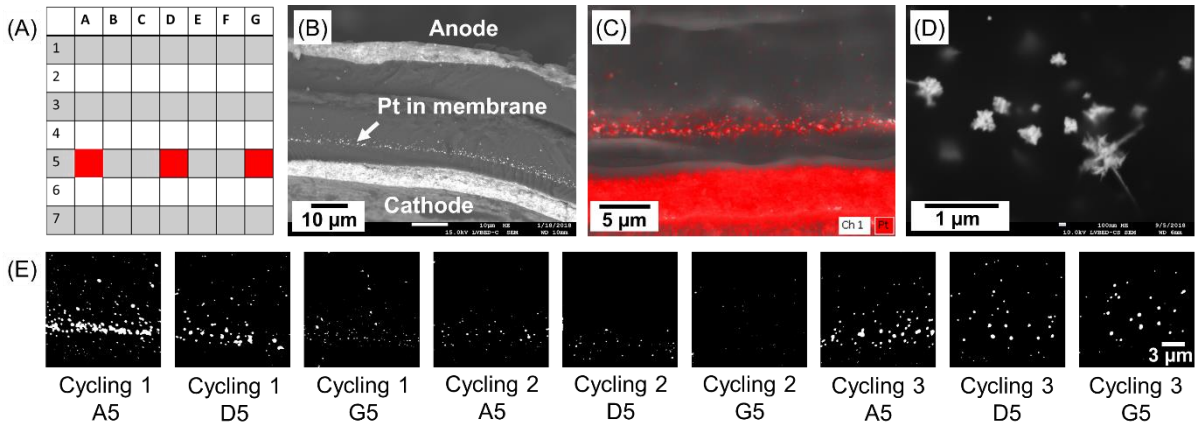

Figure 6: (A) Sketch of the segments analyzed by SEM. (B) Large area SEM BSE image of freeze fractured MEA at segment A5 after Cycling 1. (C) EDX Pt mapping at segment A5 after Cycling 1. (D) Higher magnification of the Pt particles at segment A5 after Cycling 1. (E) Binarized SEM BSE images of the Pt-band (Pt visible as white spots) in segments A5, D5 and G5 after the individual cycling tests.

The results of the average platinum area fraction of the image measured in front of the cathode are shown in *Figure 7* with the standard error of the mean of six areas. The platinum area fraction taken as a measure for the Pt content is comparable for Cycling 1 and Cycling 3. The platinum content measured in the MEA after operation with Cycling 2 is considerably lower than for the two other MEAs. The Cycling 2 protocol did not include OCV condition which is known to be harsh for the stability of the Pt and carbon in the electrodes. The platinum content in the segments follows the same order for all MEAs: The highest Pt content was always measured in segments A5, less in segments D5 and the lowest content was detected in G5 segments. In other words, Pt band formation (or Pt dissolution in the catalyst layer) is not homogenous but increases from air inlet to air outlet. Humidification increases at air outlet due to accumulation of product water closer to the outlet area, which increases the mobility of the platinum ions in the membrane. As the cell was operated in co-flow

the hydrogen concentration might be lower at the outlet area which results in a lower amount of Pt^{2+} reduction.

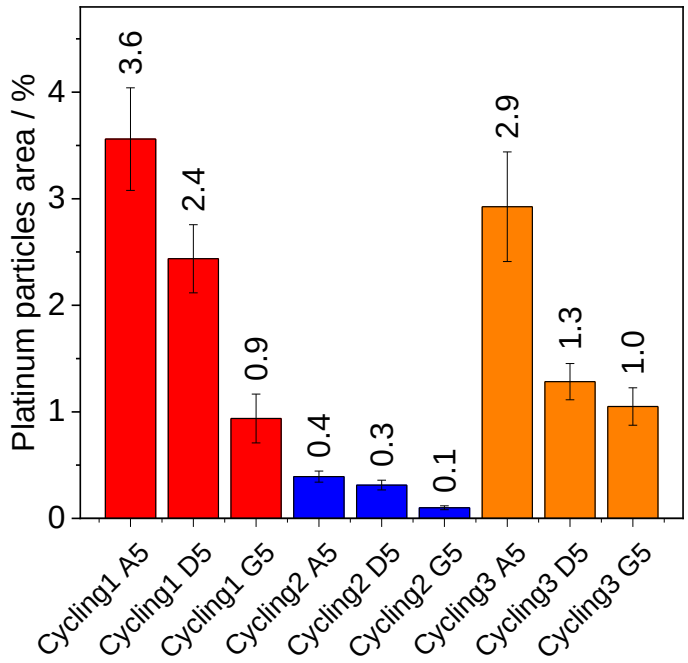

Figure 7: Average platinum area fraction in front of the cathodes (six measurements with 15x15 µm² each at the membrane in front of the cathode), error bars indicate the standard error of the mean for 6 measurements.

Further analysis has been performed by correlating the current density distributions obtained from the polarization curves with the amount of Pt determined in the corresponding segment. Comparing the current density recorded in the analyzed segments during the cycling tests suggests that with higher local current density during operation more Pt is detected in the membrane. This observation is valid for current density recorded at high load (see Figure 6S in the supporting information): High load means that cell is stronger humidified and becomes more prone to mass transport losses. This effect becomes further reinforced by the decreased cathode

thickness due to Pt dissolution and Pt and formation Therefore, for low loads, no corresponding correlation was found. The correlation between measured current densities and Pt content is clearly valid for Cycling 1 and Cycling 2. In Cycling 3 the trend is less clear.

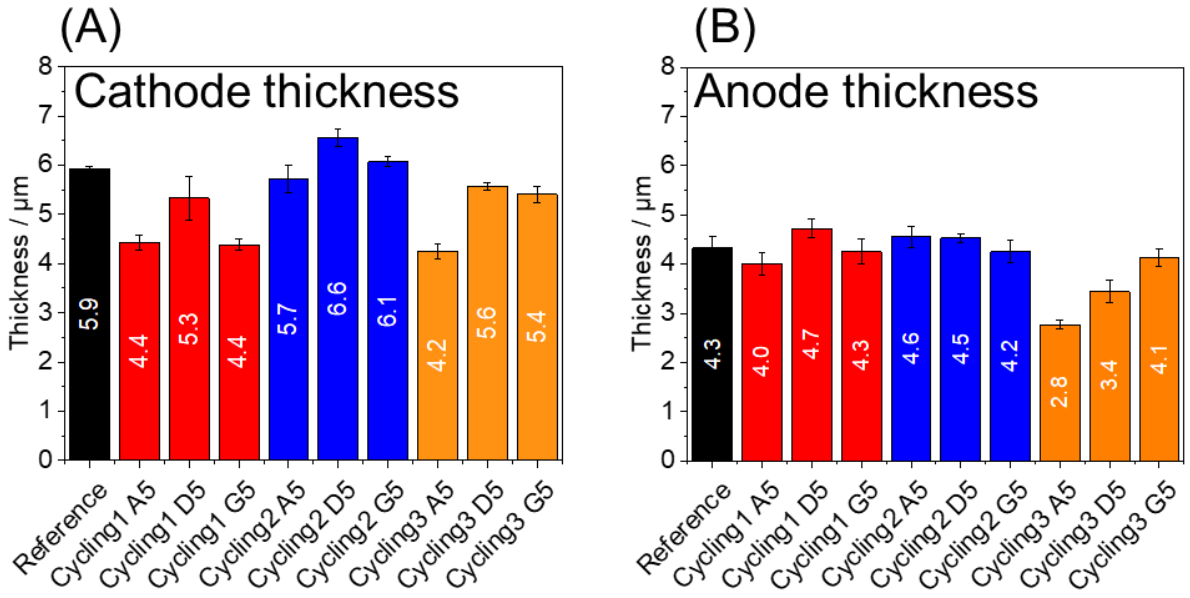

Figure 8: Thicknesses of electrode components determined from SEM cross sections. (A) Thickness of a new cathode and of aged cathodes samples after Cycling 1, Cycling 2, and Cycling 3 analyzed at the indicated segments, the error bars indicate the standard error of the mean for 6 measurements. (B) Thickness of a new anode and of aged anode samples after Cycling 1, Cycling 2, and Cycling 3 analyzed at the indicated segments, the error bars indicate the standard error of the mean for 6 measurements.

The thickness of the cathodes at the different segments decreased for MEAs that were operated with OCV included in the protocol, i.e. MEAs of Cycling 1 and Cycling 3 (see Figure 8 (A)). The decrease of cathode thickness after operation was largest after Cycling 1 and Cycling 3 at segments A5, where also the highest amount of platinum was measured in the membrane (compare Figure 7) indicating a relation

between Pt dissolution on the cathode catalyst layer and Pt band formation The change in cathode thickness of Cycling 2 is not significant.

The MEAs after Cycling 1 and Cycling 2 showed no significant thickness change of the anodes which are expected due to low anode potentials during operation. Only the anode of the MEA after Cycling 3 test shows a clear decrease of the thickness (Figure 8 (B)). These observations are consistent with the fact that only for the MEA of Cycling 3 platinum was detected in the membrane close to the anode side. One possibility for the platinum particles close to the anode side could be the higher current range which enables a further movement of the Pt-ions.

4. Conclusions

The impact of load cycling on PEMFC degradation was studied based on three durability tests with different current ranges of operation (0.0-0.2 Acm^{-2}, 0.2-1.0 Acm^{-2} and 0.0-1.0 Acm^{-2}). The results were additionally compared with tests performed at steady state conditions.

The results clearly show that dynamic operation leads to lower performance losses compared to operation at constant current. This can become issues for PEMFC in heavy duty applications where 1) particularly high durability is required and 2) less dynamics is expected compared to automotive driving profiles. Among the cycling tests, the one with operation in the low current range (i.e. high voltage range) exhibited highest irreversible and reversible degradation which is caused by a significantly increased HFR and LFR due to membrane degradation and carbon corrosion and Pt dissolution. The observed performance losses are closely linked with inhomogeneous current density distributions. These inhomogeneities are partly

reversible. Nevertheless, the regions that experience relatively high local current densities develop a Pt band in the membrane which is correlated with irreversible cathode degradation. Since Pt redeposited in the membrane is known to affect membrane degradation [13, 60], the results suggest that maintaining a homogenous current density distribution during operation is beneficial or even necessary to avoid local degradation issues. Interestingly, membrane thinning was observed only after the cycling tests not including OCV. It is speculated that in the tests including OCV the density of Pt precipitates in the membrane was higher, thus preventing membrane degradation.

5. Acknowledgments

This project has received funding from the Fuel Cells and Hydrogen 2 Joint Undertaking under grant agreement No 779565 (ID-Fast) and No 779550 (PEGASUS). This Joint Undertaking receives support from the European Union's Horizon 2020 research and innovation program.

6. References

[1] https://www.fch.europa.eu/page/multi-annual-work-plan

[2] https://www.energy.gov/eere/fuelcells/doe-technical-targets-fuel-cell-systems-and-stacks-transportation-applications

[3] R. Borup, J. Meyers, B. Pivovar, Y.S. Kim, R. Mukundan, N. Garland, et al., Scientific aspects of polymer electrolyte fuel cell durability and degradation., Chem. Rev. 107 (2007) 3904.

[4] https://www.energy.gov/eere/fuelcells/doe-technical-targets-fuel-cell-systems-and-stacks-transportation-applications

[5] https://www.fch.europa.eu/sites/default/files/S4_Panel%202_Caloprisco%20final.pdf

[6] O. T. Holton and J. W. Stevenson, “The Role of Platinum in Proton Exchange Membrane Fuel Cells,” *Platin. Met. Rev.*, vol. 57, no. 4, pp. 259–271, 2013.

[7] P. Gazdzicki, J. Mitzel, D. Garcia Sanchez, M. Schulze, and K. A. Friedrich, “Evaluation of reversible and irreversible degradation rates of polymer electrolyte membrane fuel cells tested in automotive conditions,” *J. Power Sources*, vol. 327, pp. 86–95, 2016.

[8] Jundika C.Kurnia, Agus P.Sasmito, Tariq Shamim. Performance evaluation of a PEM fuel cell stack with variable inlet flows under simulated driving cycle conditions. Appl Energy Volume 206, 15 November 2017, Pages 751-764

[9] W. Schmittinger and A. Vahidi, “A review of the main parameters influencing long-term performance and durability of PEM fuel cells,” *J. Power Sources*, vol. 180, no. 1, pp. 1–14, 2008.

[10] N. Ramaswamy, N. Hakim, and S. Mukerjee, “Degradation mechanism study of perfluorinated proton exchange membrane under fuel cell operating conditions,” *Electrochim. Acta*,vol 53, pp3279-3295, 2008.

[11] A. Kongkanand J. Zhang, Z. Liu, YH Lai, P.Sinha, E. L. Thompson and R.Makharia. “Degradation of PEMFC Observed on NSTF Electrodes,” J.Electrochem. Soc., vol. 161, no. 6, pp. F744–F753, 2014.

[12] F. A. De Bruijn, V. A. T. Dam, and G. J. M. Janssen, “Review: Durability and degradation issues of PEM fuel cell components,” *Fuel Cells*, vol. 8, no. 1, pp. 3–22, 2008.

[13] S. Helmly, B. Ohnmacht, P. Gazdzicki, R. Hiesgen, E. Gülzow, and K. A. Friedrich, “Influence of the Distribution of Platinum Deposits on the Properties and Degradation of Platinum-Impregnated Nafion Membranes,” *J. Electrochem. Soc.* vol. 161 no14, pp. 1416-1426, 2014.

[14] S. Kundu, M. Fowler, L. C. Simon, and R. Abouatallah, “Reversible and irreversible degradation in fuel cells during Open Circuit Voltage durability testing,” *J. Power Sources*, vol. 182, no. 1, pp. 254–258, 2008.

[15] A. Panchenko, H. Dilger, E. Möller, T. Sixt, and E. Roduner, “In situ EPR investigation of polymer electrolyte membrane degradation in fuel cell applications,” in *Journal of Power Sources*, vol. 127, no. 1-2, pp. 325–330, 2004.

[16] R. Petrone, D. Hissel, M. C. Péra, D. Chamagne, and R. Gouriveau, “Accelerated stress test procedures for PEM fuel cells under actual load constraints: State-of-art and proposals,” *Int. J. Hydrogen Energy*, vol. 40, no. 36, pp. 12487-12505, 2015.

[17] M. Kim *et al.*, “Effects of anode flooding on the performance degradation of polymer electrolyte membrane fuel cells,” *J. Power Sources*, vol. 266, no. 15, pp. 332–340, 2014.

[18] S. Enz, T. A. Dao, M. Messerschmidt, and J. Scholta, “Investigation of degradation effects in polymer electrolyte fuel cells under automotive-related operating conditions,” *J. Power Sources*, vol. 274, no. 15, pp. 521–535, 2015.

[19] M. Schulze, N. Wagner, T. Kaz, and K. A. Friedrich, “Combined electrochemical and surface analysis investigation of degradation processes in polymer electrolyte membrane fuel cells,” *Electrochim. Acta*, vol. 52, no. 6, pp. 2328–2336, 2007.

[20] Salah Laghrouche, Jianxing Liu, Fayez Shakil Ahmed, Mohamed Harmouche, and Maxime Wack._Adaptive Second-Order Sliding Mode Observer-Based Fault Reconstruction for PEM Fuel Cell Air-Feed System IEEE Transactions on Control Systems Technology, 23(3):1098-1109, 2015;

[21] Jianxing Liu, Yabin Gao, Xiaojie Su, Maxime Wack, and Ligang Wu , Disturbance-Observer-Based Control for Air Management of PEM Fuel Cell Systems via Sliding Mode Technique. IEEE Transactions on Control Systems Technology, vol. 27, no. 3, pp. 1129–1138, 2019;

[22] Jianqiu Mu, Xing-Gang Yan, Sarah K. Spurgeon, and Zehui Mao. Generalized Regular Form Based SMC for Nonlinear Systems With Application to a WMR IEEE TIE, 63(5): 3261-3270, 2016.

[23] L. C. Pérez, L. Brandão, J. M. Sousa, and A. Mendes, “Segmented polymer electrolyte membrane fuel cells-A review,” *Renewable and Sustainable Energy Reviews*. vol. 15, no. 1, 169-185, 2011.

[24] J. Stumper, S. A. Campbell, D. P. Wilkinson, M. C. Johnson, and M. Davis, “In-situ methods for the determination of current distributions in PEM fuel cells,” *Electrochim. Acta*, vol. 43, no. 24, 3773-3783, 1998.

[25] M. Noponen, T. Mennola, M. Mikkola, T. Hottinen, and P. Lund, “Measurement of current distribution in a free-breathing PEMFC,” in *Journal of Power Sources*, vol. 106, no.1-2, 304-312, 2002.

[26] Y. G. Yoon, W. Y. Lee, T. H. Yang, G. G. Park, and C. S. Kim, “Current distribution in a single cell of PEMFC,” *J. Power Sources*, vol. 118, no. 1–2, pp. 193–199, 2003.

[27] J. J. Hwnag, W. R. Chang, R. G. Peng, P. Y. Chen, and A. Su, “Experimental and numerical studies of local current mapping on a PEM fuel cell,” *Int. J. Hydrogen Energy*, vol. 33, no.20, 5718-5727, 2008.

[28] M. Schulze, E. Gülzow, S. Schönbauer, T. Knöri, and R. Reissner, “Segmented cells as tool for development of fuel cells and error prevention/prediagnostic in fuel cell stacks,” *J. Power Sources,* vol. 173, no.1,8, 19-27, 2007.

[29] F. N. Büchi, A. B. Geiger, and R. P. Neto, “Dependence of current distribution on water management in PEFC of technical size,” *J. Power Sources*, vol. 145, no.1,4, 62-67, 2005.

[30] F. B. Weng, B. S. Jou, C. W. Li, A. Su, and S. H. Chan, “The effect of low humidity on the uniformity and stability of segmented PEM fuel cells,” *J. Power Sources*, vol. 181, no.2, 251-258, 2008.

[31] D. G. Sanchez and P. L. Garcia-Ybarra, “PEMFC operation failure under severe dehydration,” in *International Journal of Hydrogen Energy*, vol. 37, no.8, 7279-7288, 2012.

[32] D. G. Sanchez, D. G. Diaz, R. Hiesgen, I. Wehl, and K. A. Friedrich, “Oscillations of PEM fuel cells at low cathode humidification,” *J. Electroanal. Chem.* vol. 649, no. 1–2, pp. 219–231, 2010.

[33] D. G. Sanchez , A. Ortiz, K. A. Friedrich “Oscillation of PEFC under Low Cathode Humidification: Effect of Gravitation and Bipolar Plate Design,” *J. Electrochem. Soc.* vol. 160, no. 6, pp. 636–644, 2013.

[34] D. G. Sanchez, T. Ruiu, K. A. Friedrich, J. Sanchez-Monreal, and M. Vera, “Analysis of the Influence of Temperature and Gas Humidity on the Performance Stability of Polymer Electrolyte Membrane Fuel Cells,” *J. Electrochem. Soc.* vol. 163, no. 3, pp. 150–159, 2016.

[35] P. A. García-Salaberri, D. G. Sánchez, P. Boillat, M. Vera, and K. A. Friedrich, “Hydration and dehydration cycles in polymer electrolyte fuel cells operated with wet anode and dry cathode feed: A neutron imaging and modeling study,” *J. Power Sources*, vol. 359, pp. 634–655, 2017.

[36] T. V. Reshetenko, G. Bender, K. Bethune, and R. Rocheleau, “Systematic studies of the gas humidification effects on spatial PEMFC performance distributions,” *Electrochim. Acta*, vol. 69, pp. 220-229, 2012.

[37] K. Panha, M. Fowler, Xiao-ZiYuan, H.Wang. Accelerated durability testing via reactants relative humidity cycling on PEM fuel cells. Applied Energy Volume 93, May 2012, Pages 90-97

[38] D. G. Sanchez, T. Ruiu, I. Biswas, M. Schulze, S. Helmly, and K. A. Friedrich, “Local impact of humidification on degradation in polymer electrolyte fuel cells,” *J. Power Sources*, vol. 352, pp. 42–55, 2017.

[39] T. V. Reshetenko and J. St-Pierre, “Study of acetylene poisoning of Pt cathode on proton exchange membrane fuel cell spatial performance using a segmented cell system,” *J. Power Sources*, vol. 287,no. 2, pp. 401-415, 2015.

[40] D. Liang, Q. Shen, M. Hou, Z. Shao, and B. Yi, “Study of the cell reversal process of large area proton exchange membrane fuel cells under fuel starvation,” *J. Power Sources*, vol. 194, pp. 4847-853, 2009

[41] M. Dou *et al.*, “Behaviors of proton exchange membrane fuel cells under oxidant starvation,” *J. Power Sources*, vol. 196,no. 5, pp. 2759-2762, 2011.

[42] Z. Liu, L. Yang, Z. Mao, W. Zhuge, Y. Zhang, and L. Wang, “Behavior of PEMFC in starvation,” *J. Power Sources*, vol. 157,no. 1, pp. 166-176, 2006.

[43] T. V. Reshetenko, G. Bender, K. Bethune, and R. Rocheleau, “Systematic study of back pressure and anode stoichiometry effects on spatial PEMFC performance distribution,” *Electrochim. Acta*, vol. 56,no. 24, pp. 8700-8710, 2011.

[44] T. V. Reshetenko, G. Bender, K. Bethune, and R. Rocheleau, “Effects of local variations of the gas diffusion layer properties on PEMFC performance using a segmented cell system,” *Electrochim. Acta*, vol. 80, pp. 368-376, 2012.

[45] T. V. Reshetenko, J. St-Pierre, and R. Rocheleau, “Effects of local gas diffusion layer gas permeability variations on spatial proton exchange membrane fuel cells performance,” *J. Power Sources*, vol. 241,no. 1, pp. 597-607, 2013.

[46] R. Lin, E. Gülzow, M. Schulze, and K. A. Friedrich, “Investigation of Membrane Pinhole Effects in Polymer Electrolyte Fuel Cells by Locally Resolved Current Density,” *J. Electrochem. Soc.* vol. 158 ,no. 1, pp. 11-17, 2011.

[47] T. V. Reshetenko, G. Bender, K. Bethune, and R. Rocheleau, “Application of a segmented cell setup to detect pinhole and catalyst loading defects in proton exchange membrane fuel cells,” *Electrochim. Acta*, vol.76, pp.16-25, 2012.

[48] B. Martinez-Vazquez, D. G. Sanchez, J. L. Castillo, K. A. Friedrich, and P. L. Garcia-Ybarra, “Scaling-up and characterization of ultralow-loading MEAs made-up by electrospray,” *Int. J. Hydrogen Energy*, vol. 40,no. 15, pp. 5384-5389, 2015.

[49] G. S. Harzer, J. N. Schwämmlein, A. M. Damjanović, S. Ghosh, and H. A. Gasteiger, “Cathode Loading Impact on Voltage Cycling Induced PEMFC Degradation: A Voltage Loss Analysis,” *J. Electrochem. Soc.* vol. 165,no. 6, pp. 3118-3131, 2018.

[50] P. Zihrul, I. Hartung, S. Kirsch, G. Huebner, F. Hasché, and H. A. Gasteiger, “Voltage Cycling Induced Losses in Electrochemically Active Surface Area and in H_2 /Air-Performance of PEM Fuel Cells,” *J. Electrochem. Soc.*, vol. 163, no. 6, pp. F492–F498, 2016.

[51] K. Yu *et al.*, “Degradation mechanisms of Platinum Nanoparticle Catalysts in Proton Exchange Membrane Fuel Cells : The Role of Particle Size,” *Chem. Mater.*, vol. 26, pp. 5540–5548, 2014.

[52] R. K. Ahluwalia *et al.*, “Dynamics of Particle Growth and Electrochemical Surface Area Loss due to Platinum Dissolution,” *J. Electrochem. Soc.*, vol. 161, no. 3, pp. 291–304, 2014.

[53] S. Arisetty, X. Wang , R. K. Ahluwalia, R. Mukundan , R. Borup, J. Davey, D. Langlois, F. Gambini, O. Polevaya,* and S. Blanchet “Catalyst Durability in PEM Fuel Cells with Low Platinum Loading,” J. Electrochem. Soc., vol. 159, no. 5, p. B455, 2012.

[54] T. Kaz and H. Sander. “Device for measuring local current/heat distribution on electrochemical electrode has current flow direction to resistance element transverse to current flow direction to current conducting element,” DE10316117 B3, 2004.

[55] T. Kaz and H. Sander. “Measurement of the current distribution/heat distribution of an electrochemical electrode,” EP1618395 A1, 2006.

[56] J. Wu, X. Zi Yuana, J. J. Martin, H. Wang, J. Zhang, J. Shen, S. Wu and W. Merida "A review of PEM fuel cell durability: Degradation mechanisms and mitigation strategies", J. Power Sources, vol 184, no. 1, pp. 104-119, 2008.

[57] Y., ShaoGeping and Y. Gao, "Understanding and approaches for the durability issuesof Pt-based catalysts for PEM fuel cell", J. Power Sources 171,pp. 558–566, 2007.

[58] X.P. Wang, R. Kumar and D.J. Myers, "Effect of Voltage on Platinum Dissolution Relevance to Polymer Electrolyte Fuel Cells", Electrochem. Solid-State Lett., vol. 9, issue 5, pp. A225-A227, 2006.

[59] L. Kim, C. G. Chung, Y. W. Sung, and J. S. Chung, “Dissolution and migration of platinum after long-term operation of a polymer electrolyte fuel cell under various conditions,” *J. Power Sources*, vol. 183, no. 2, pp. 524–532, 2008.

[60] S. Helmly, R. Hiesgen, T. Morawietz, X.-Z. Yuan, H. Wang, and K. Andreas Friedrich, “Microscopic Investigation of Platinum Deposition in PEMFC Cross-Sections Using AFM and SEM,” *J. Electrochem. Soc.* vol. 160, no. 6, pp. 687–697, 2013.

[61] L. Tang *et al.*, “Electrochemical stability of nanometer-scale Pt particles in

acidic environments," *J. Am. Chem. Soc.*, vol. 132, pp. 596–600, 2010.

[62] H. Liu, J. Zhang, F. D. Coms, W. Gu, B. Litteer, and H. A. Gasteiger, "Impact of Gas Partial Pressure on PEMFC Chemical Degradation," *ECS Trans.* vol. 3, pp. 493-505, 2006.

Supporting Information

Local impact of load cycling on degradation mechanism in polymer electrolyte fuel cells

D. Garcia-Sanchez[1*], T. Morawietz[2], Pedro Gama da Rocha[1], R. Hiesgen[2], Pawel Gazdzicki[1], K. A. Friedrich[1,3]

[1] German Aerospace Center (DLR), Institute of Engineering Thermodynamics, Pfaffenwaldring 38-40, 70569 Stuttgart, Germany

[2]University of Applied Sciences Esslingen, Department of Basic Science, 73728 Esslingen, Germany

3 University of Stuttgart, Institute of Building Energetics, Thermal Engineering and Energy Storage (IGTE), Pfaffenwaldring 31, 70569 Stuttgart, Germany

*corresponding author: Daniel.GarciaSanchez@dlr.de

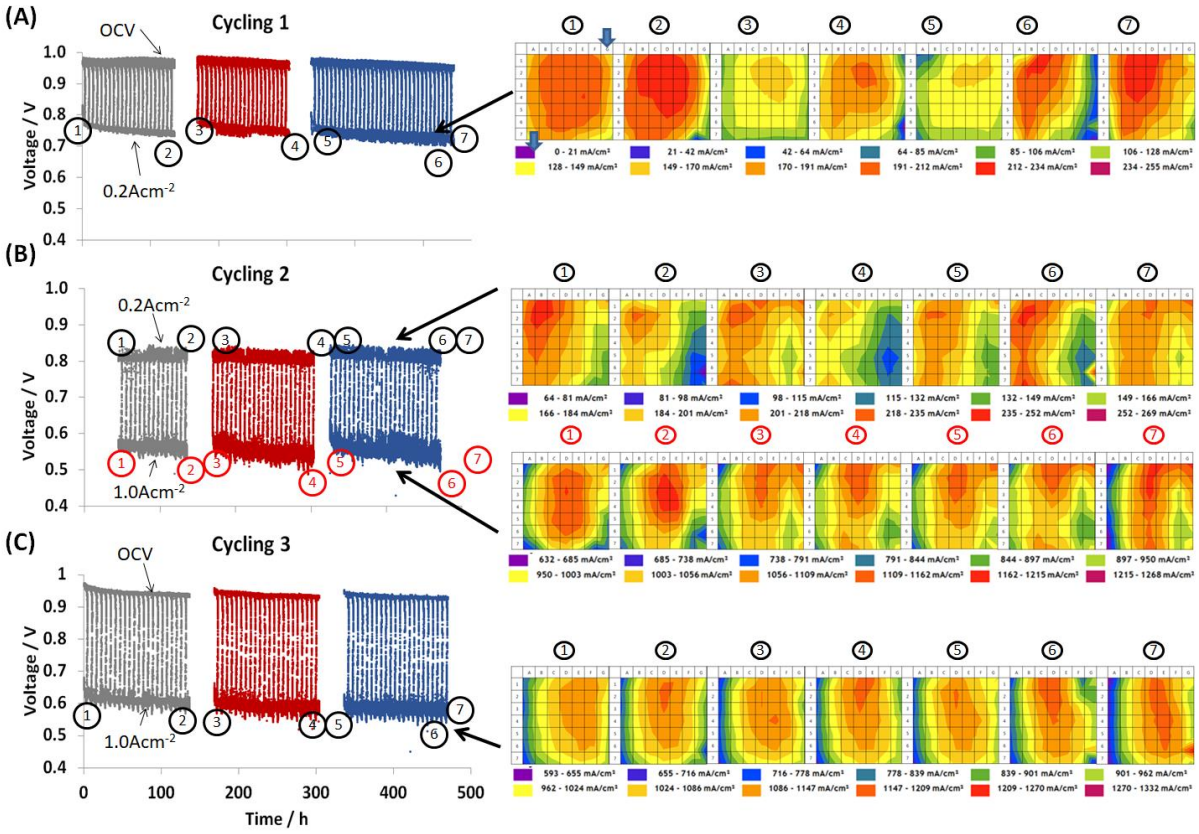

Figure 15: (Left:) Cell voltage versus test duration recorded using the load profiles Cycling 1 (A), Cycling 2 (B), and Cycling 3 (C). (Right:) Corresponding current density distributions recorded during the test at BoT, before and after each refresh. The assignment of the acquisition time of the current density image and the test is provided by the number labels. Gas inlet and outlet of the cell is located at segment G1 and A7, respectively.

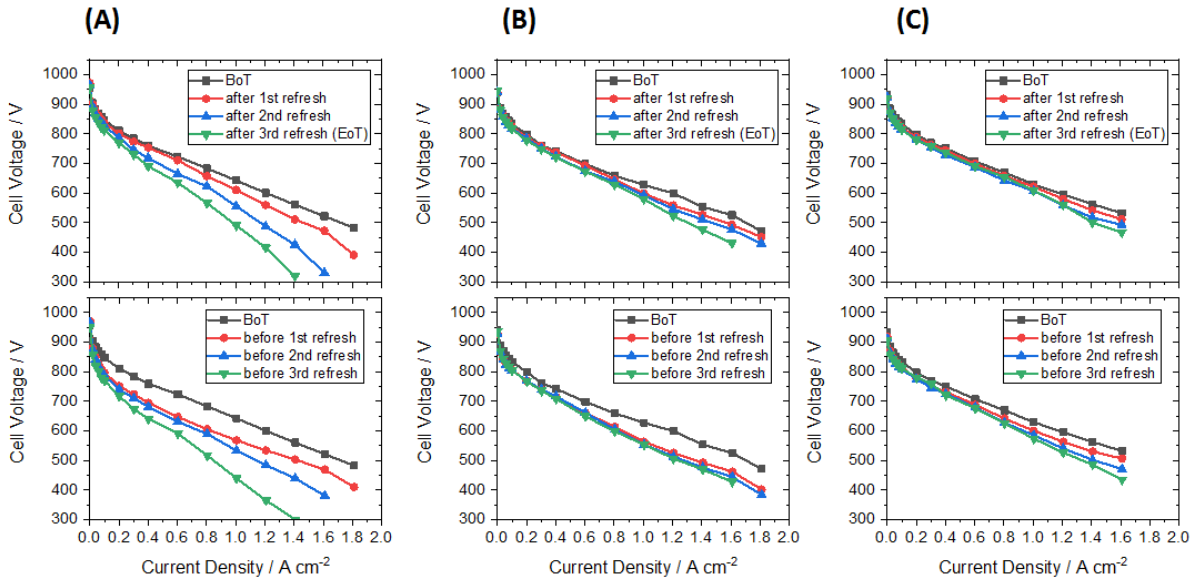

Figure 2S: (A) Performance curves recorded during Cycling 1 test. (B) Performance curves recorded during Cycling 2 test. (C) Performance curves recorded during Cycling 3 test.

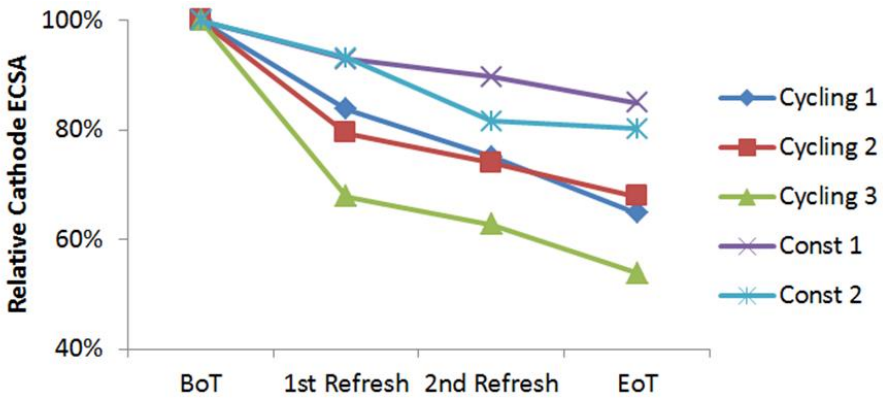

Figure 3S: Relative ECSA loss at the cathodes of the analyzed samples at BoT and after each refresh.

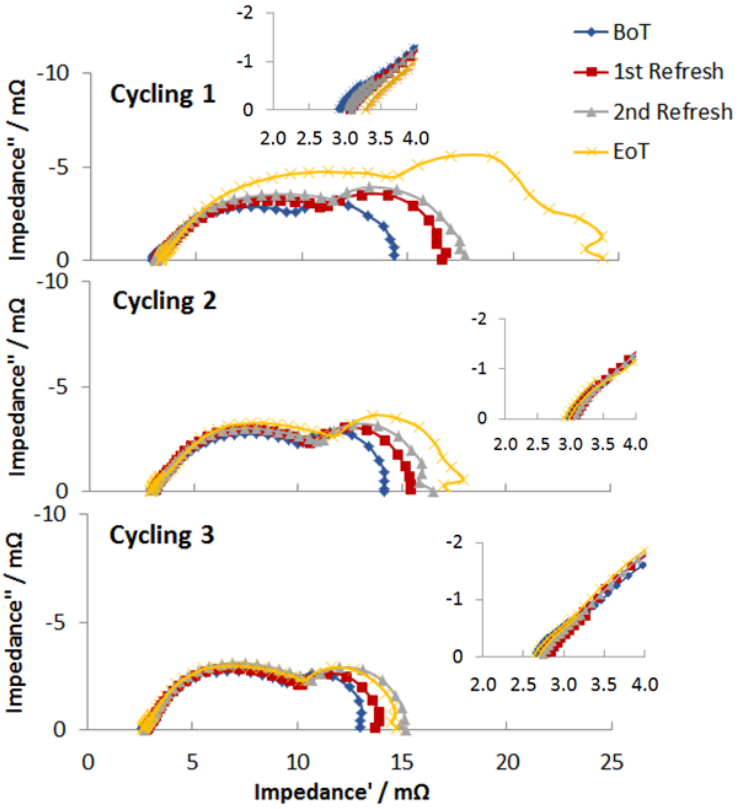

Figure 45: EIS measurements of the three cycling tests described in the main manuscript tests performed at 0.6 A cm^{-2}.

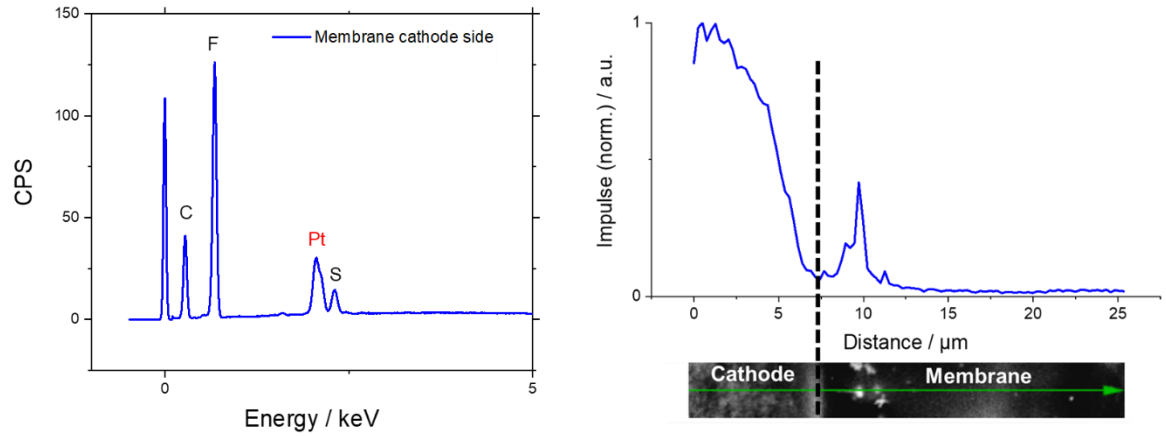

Figure 5S: EDX spectrum and EDX Pt line-scan recorded in segment A5 of the Cycling 1 test clearly showing Pt in the membrane.

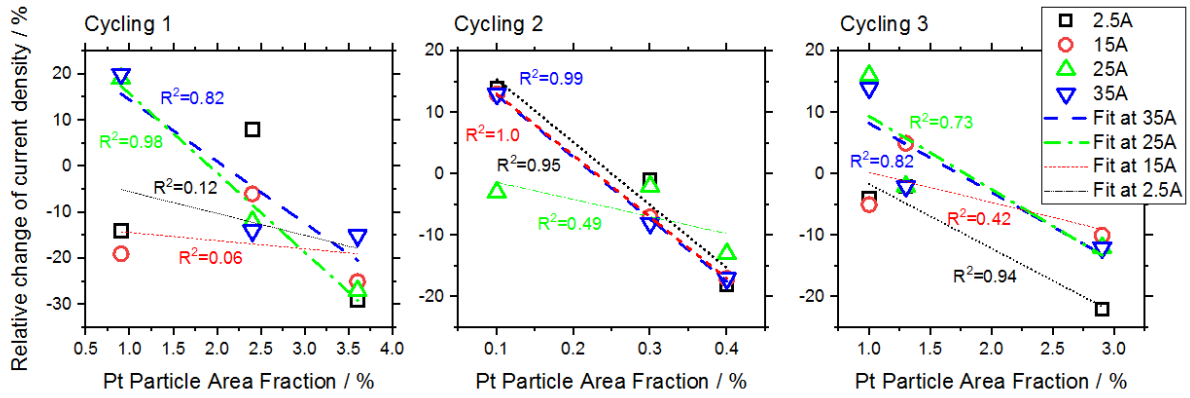

Figure 6S: Correlation of relative change of current density between BoT and EoT versus the amount of Pt detected in the membrane in the corresponding segment.

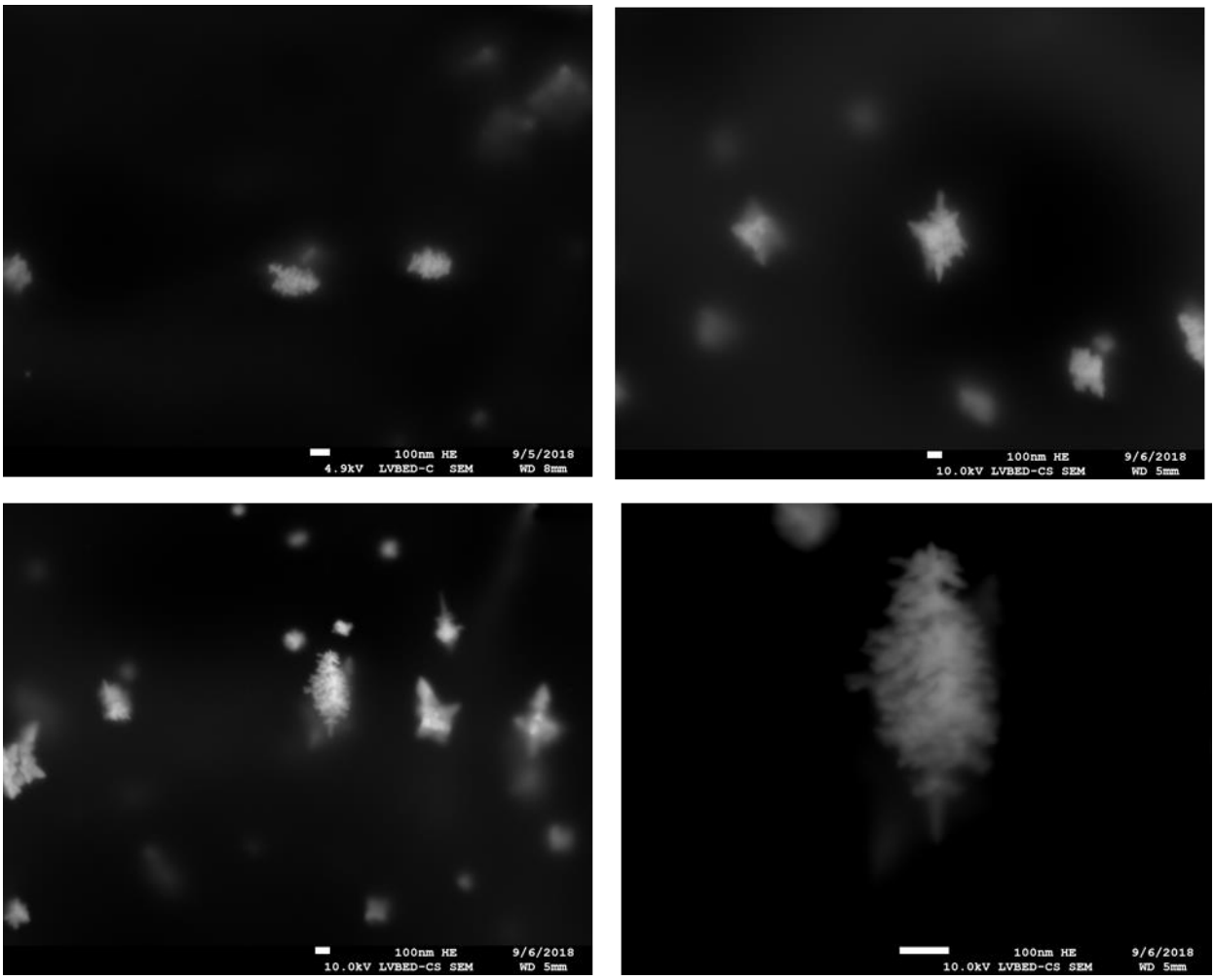

Figure 7S: SEM images of Pt precipitates in the membranes of Cycling 1 test measured in segment A5.

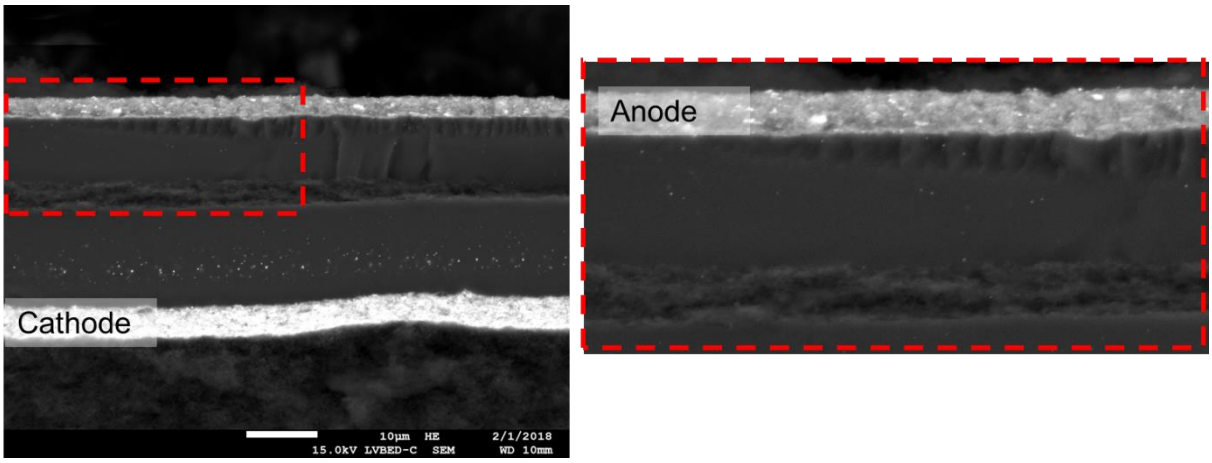

Figure 8S: SEM images of Pt precipitates in front of the anode of Cycling 3 test measured in segment A5.

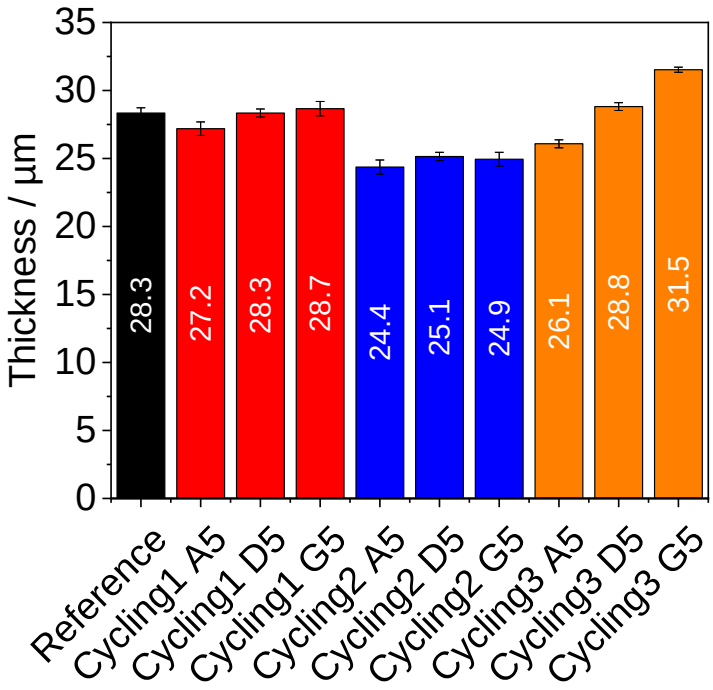

Figure 9S: Membrane thickness at EOT of the analyzed segments.

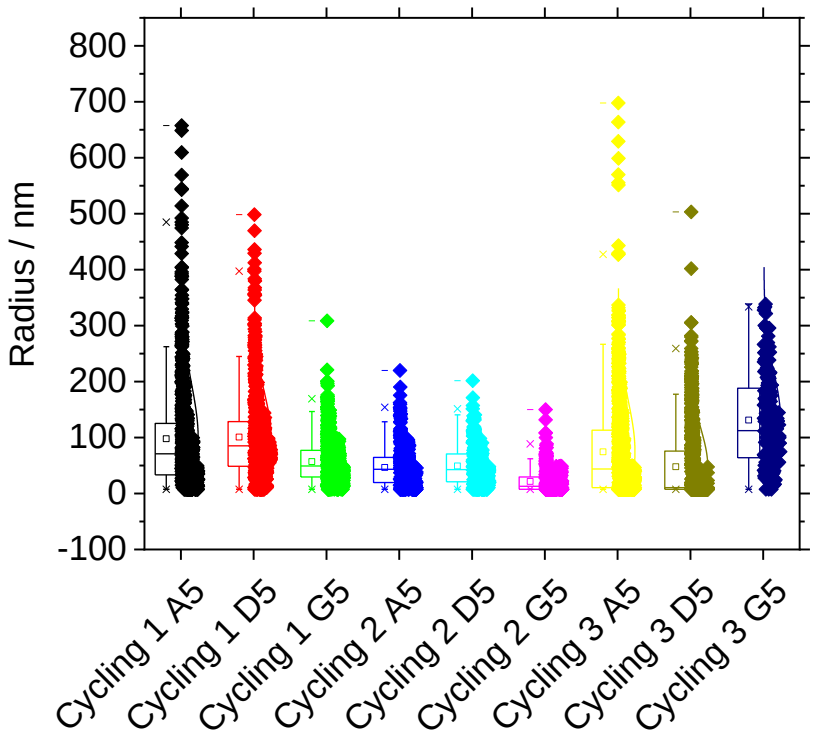

Figure 10S: Box-plots of the measured Pt-particles in the given segments.